Supplementary Information (SI) for Journal of Materials Chemistry C.

Supporting Information

Ultralow-threshold UV/solar-pumping waveguide amplifier based on Lanthanide-rich metal halide perovskite nanocrystals

Xiangbo Wang,[1] Ye Tian,[2] Joan Josep Carvajal,[3] Jing Ren,[1,4] Lu Liu,[1,4] Jianzhong Zhang[1,4]

Computational Methods

The density functional theory (DFT) calculations were carried out with the MS.[1] The exchange-correlation functional was treated within the generalized gradient approximation (GGA)[2] using the Perdew-Burke-Ernzerhof (PBE) functional hybridized with 25% exact Hartree-Fock exchange (PBE0) to achieve a more accurate description of the electronic structure. The projectoraugmented-wave pseudopotential (PAW)[3] was applied with a kinetic energy cut-off of 500 eV, which was utilized to describe the expansion of the electronic eigenfunctions. The Brillouin-zone integration was sampled by a Γ-centered 3 × 3 × 3 Monkhorst–Pack k-point. All atomic positions were fully relaxed until energy and force reached a tolerance of 1×10^{-6} eV and 0.01 eV/Å, respectively. The dispersion corrected DFT-D method was employed to consider the long-range interactions.[4] Pb^{2+} ions were substituted by a trivalent rare-earth (RE^{3+}) ion (Yb^{3+}, Er^{3+}) to simulate the doping configuration. Charge neutrality was maintained by introducing a compensating hole, corresponding to the experimental charge compensation mechanism. The *ab initio* thermodynamics approach[5] was employed to evaluate the stability and equilibrium concentration of the RE dopant.

Goldschmidt tolerance factor *t* and octahedral factor *μ*:

$$t = \frac{r_A + r_X}{\sqrt{2}\left(r_B + r_X\right)} \tag{1}$$

$$\mu = \frac{r_B}{r_X} \tag{2}$$

r_A, r_B, and r_x are the radius of corresponding ions in ABX_3 perovskite, t represents the filling condition of cation at position A, and μ represents the cation at position B in octahedron.

The calculations of PLQYs:

The photoluminescence quantum yields (PLQYs) were quantitatively determined using an integrating sphere coupled with a Horiba spectrofluorometer. The internal quantum efficiency (IQE) is defined as the percentage of the number of emitted photons to that of absorbed photons, which is calculated by the following equation:

$$\mathrm{IQE} = \frac{\int I_{\mathrm{em}}(\lambda)\cdot \mathrm{d}\lambda}{\int I_{ex}(\lambda)\cdot \mathrm{d}\lambda - \int I_{S}(\lambda)\cdot \mathrm{d}\lambda} \times 100\%$$

where I_{em} (counts) is the emission spectrum of the studied sample, I_{ex}(counts) is the spectrum of the excitation light without the sample in the sphere, and I_S is the spectrum of the excitation light after exciting the sample.

External quantum efficiency (EQE) is defined as the percentage of the number of emitted photons to that of excitation photons:

$$\mathrm{IQE} = \frac{\int I_{em}(\lambda)\cdot \mathrm{d}\lambda}{\int I_{ex}(\lambda)\cdot \mathrm{d}\lambda} \times 100\%$$

Two different detectors (PMT and InGaAs) were employed, and due to their differing responsivities, we first used a halogen lamp as the energy calibration light source to measure its visible spectral region. The theoretical near-infrared spectrum was then derived by fitting the visible spectrum with the blackbody radiation formula. The amplification coefficient was obtained by comparing the theoretical near-infrared spectrum with the spectrum measured by the InGaAs detector. By reducing the NCs concentration in the solution significantly reducing the reabsorption effect. The main uncertainties in the PLQYs measurement primarily originate from the inherent uncertainty of the standard lamp (~1–3%), and may also arise from factors such as sample positioning and light source stability. These uncertainty components were combined in quadrature (square root of the sum of squares) to obtain the standard uncertainty, estimating its combined standard uncertainty (1.94%) and expanded uncertainty (3.9%).

Table S1. ICP measurement of cation content in samples synthesized at different temperatures.

Temperature (°C)	Yb (%)	Er (%)	Pb (%)	Cs (%)
220	0.13	0.91	51.38	47.58
240	0.83	1.24	49.61	48.32
260	1.96	2.02	47.99	48.03
280	3.20	2.87	46.27	47.66
300	4.45	3.56	43.1	48.89

Table S2. Current research on the emission efficiency of $CsPbCl_3$, Yb^{3+}/Er^{3+} NCs or film at 1540 nm.

Sample	PLQY (%)	Reference
6.2%Yb^{3+}/0.8%Er^{3+}	14.6	6
1.72%Yb^{3+}/3.40%Er^{3+}	4.6	7
2.7%Yb^{3+}/2.4%Er^{3+}	6	8
6.5%Yb^{3+}/5.7%Er^{3+}	21.6	This work
37.6%Yb^{3+}/28.1%Er^{3+} (film)	30.12	9

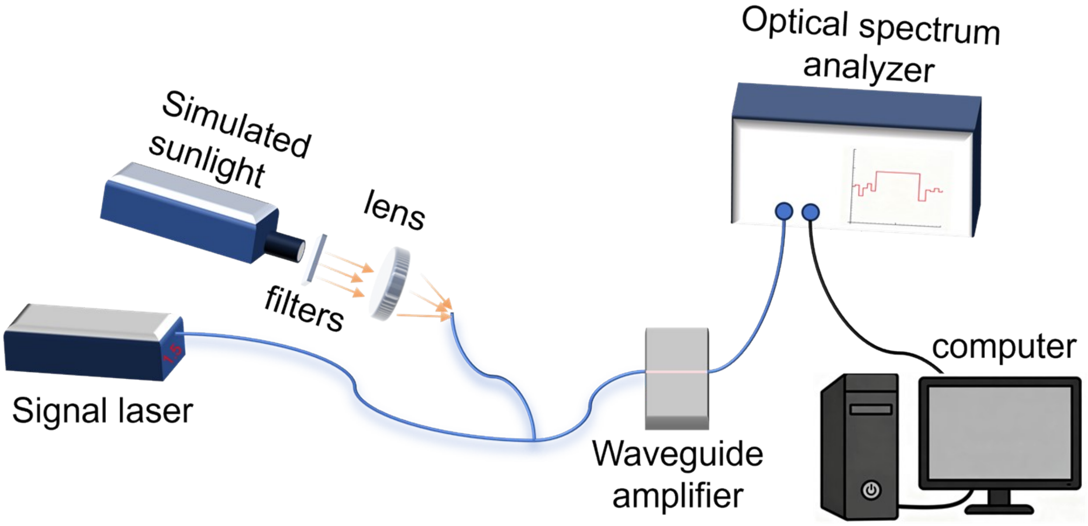

Scheme S1. Experimental setup for optical gain measurement of polymer optical waveguide amplifier. The pump light source is a 365 nm UV laser or a xenon lamp simulating sunlight. In this setup, the filter is an ultraviolet bandpass filter. The lens has a focal length of 10 mm and an aperture of 20 mm. Taking 365 nm incident light as an example, the theoretical spot size after focusing is 445.1 nm. However, due to spherical aberration, the actual spot size is 20 μm, which is still significantly smaller than the core diameter of the optical fiber used. This enables an overlap integral factor of over 0.9 between the spot and the guided mode.

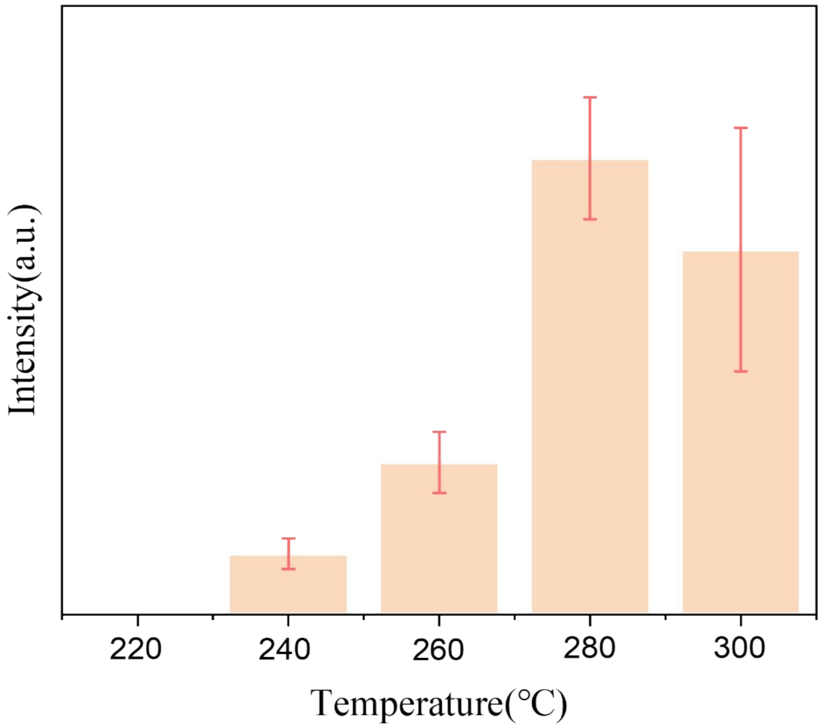

Fig. S1. PL intensity of samples from different batches synthesized via hot-injection at the same temperature.

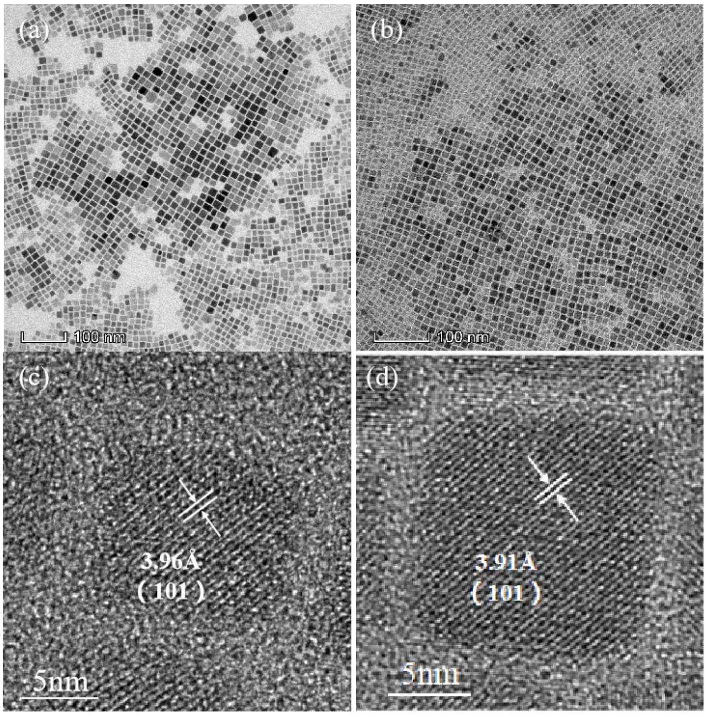

Fig. S2. TEM and HR-TEM of undoped (a, c) and CsPbCl$_3$:Yb^{3+} (b, d) NCs.

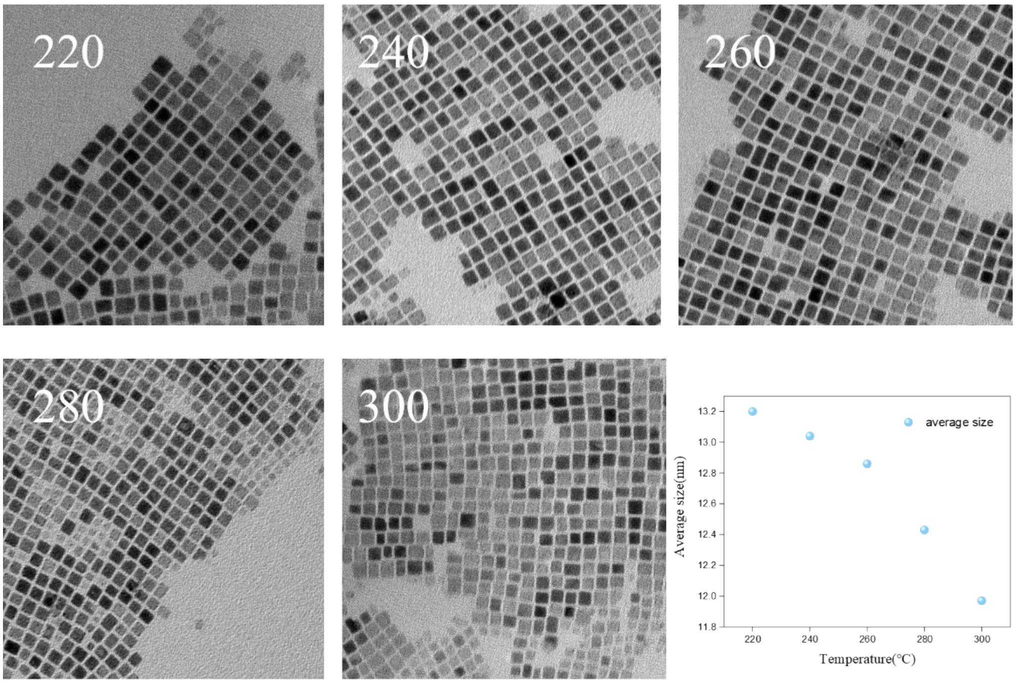

Fig. S3. Morphology and average size of nanocrystals synthesized at different temperatures.

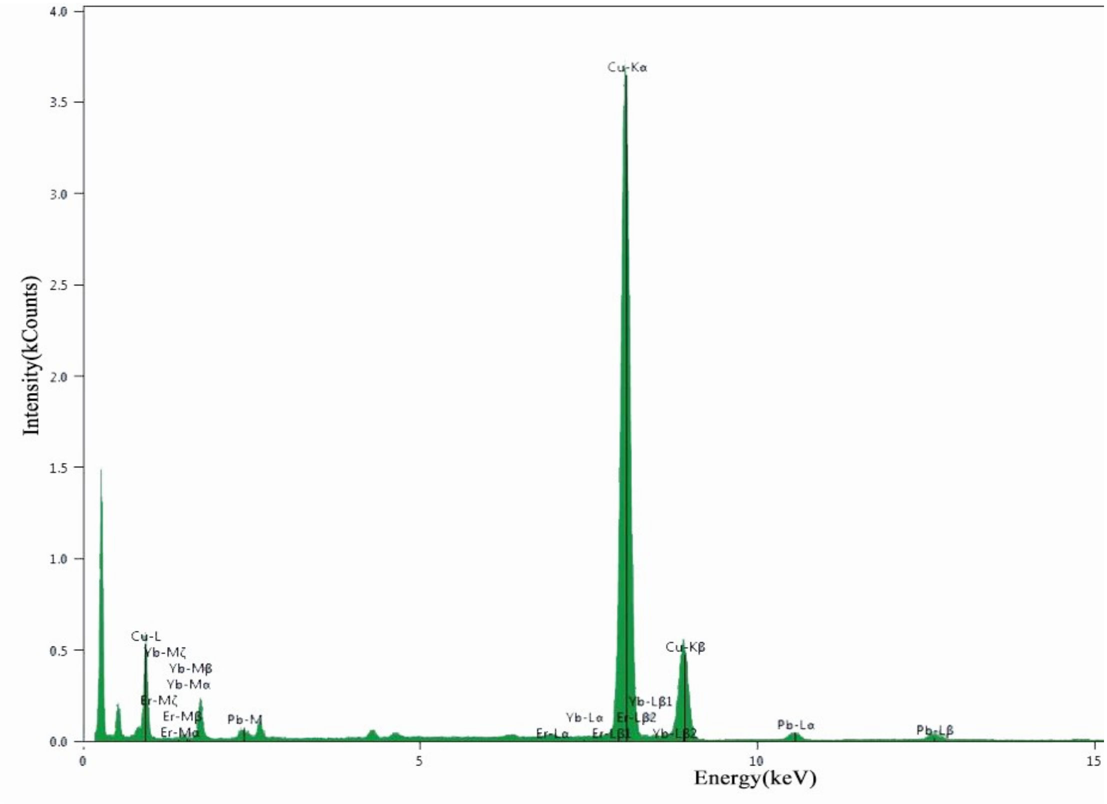

Fig. S4. The EDS pattern of $CsPbCl_3$:Yb^{3+}/Er^{3+} NCs.

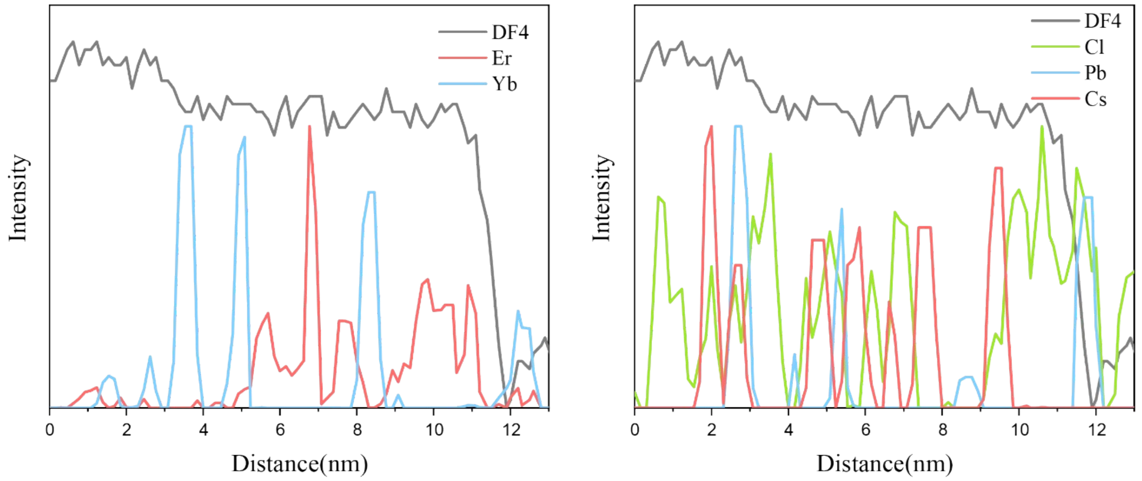

Fig. S5. STEM-EELS line scans of NCs. The line scan results for all five elements involved confirm their spatial uniformity within the NCs.

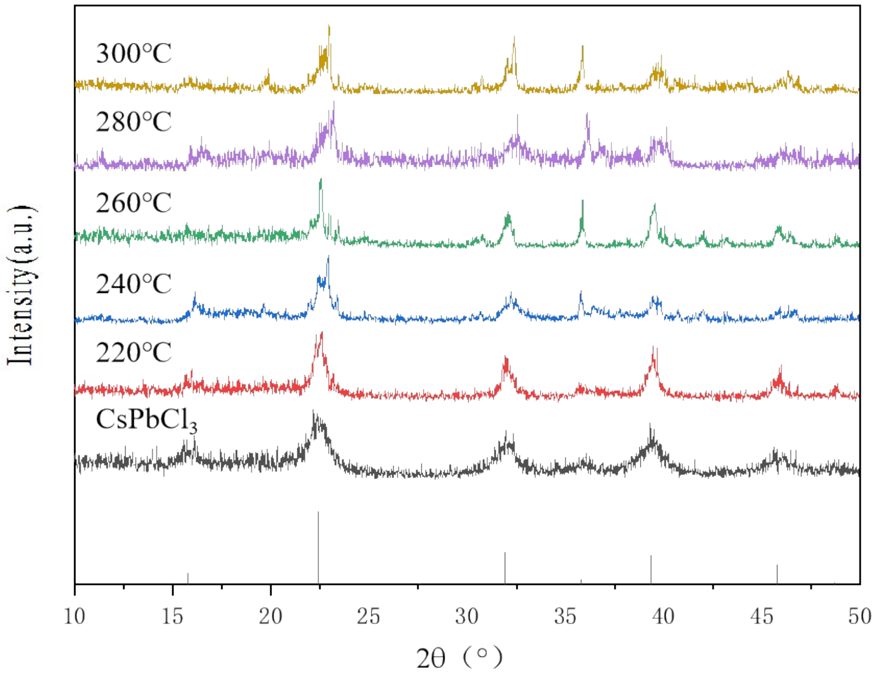

Fig. S6. XRD patterns for $CsPbCl_3:Yb^{3+}/Er^{3+}$ synthesized at various temperatures.

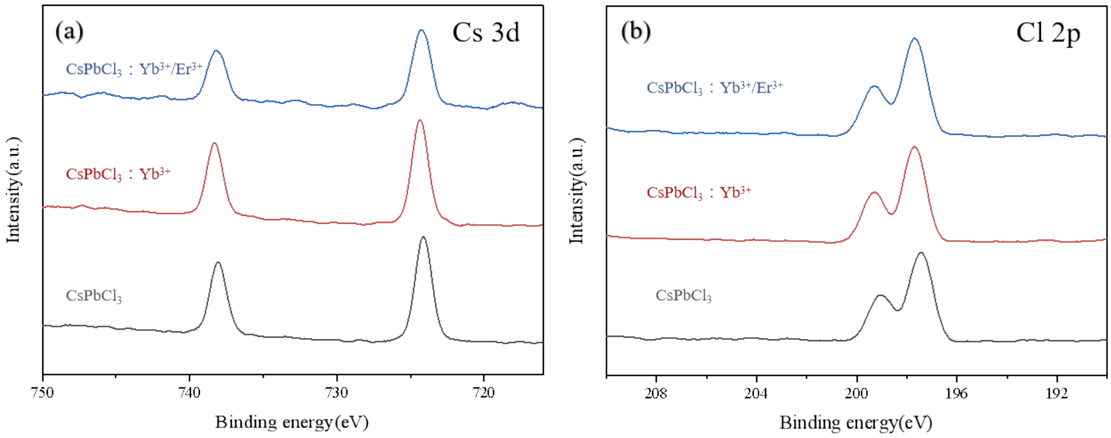

Fig. S7. XPS spectra for (a) Cs^+ 3d and (b) Cl^- 2p electrons of $CsPbCl_3$:Yb^{3+}/Er^{3+} NCs.

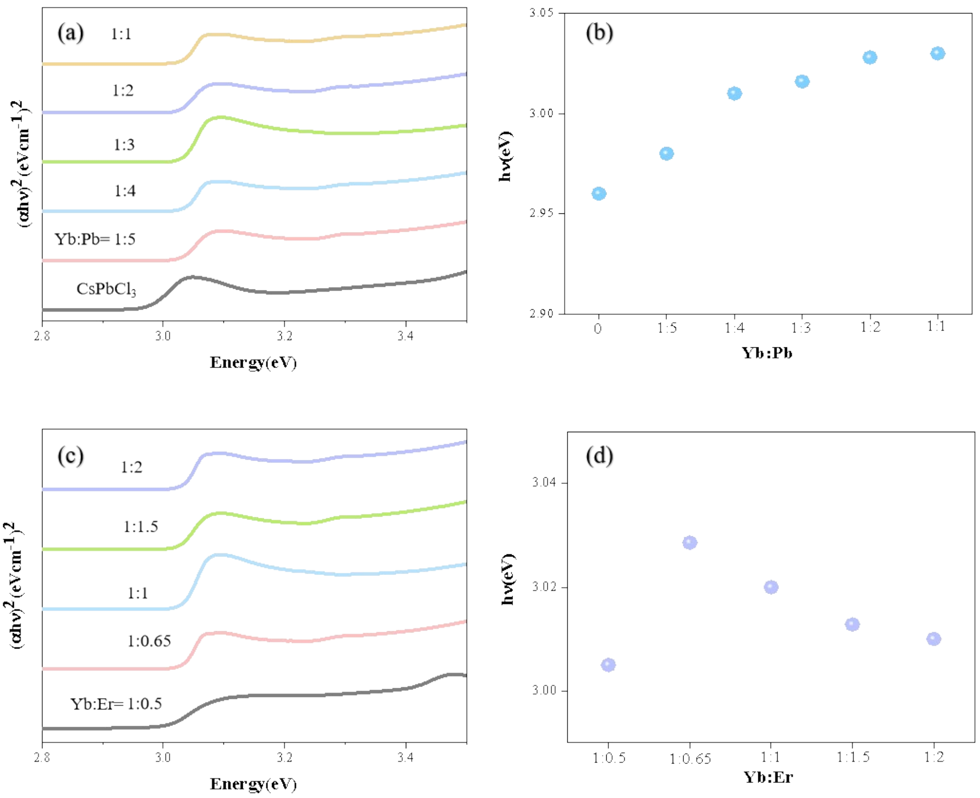

Fig. S8. Tauc plot diagrams and the corresponding bandgaps of (a, b) $CsPbCl_3:Yb^{3+}$ and (c, d) $CsPbCl_3:Yb^{3+}/Er^{3+}$ NCs.

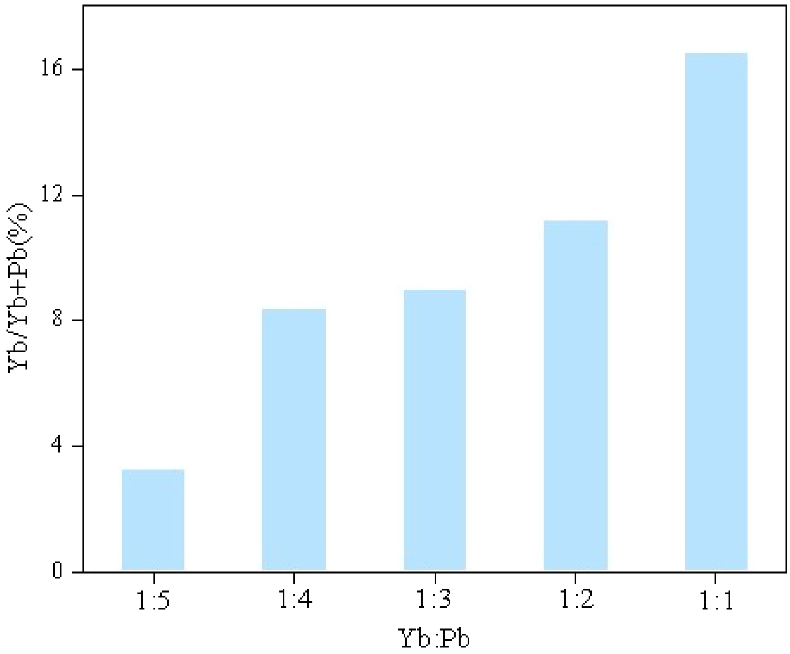

Fig. S9. Actual ion doping concentrations of $CsPbCl_3:Yb^{3+}$ NCs under the different additions of Yb^{3+} in precursors.

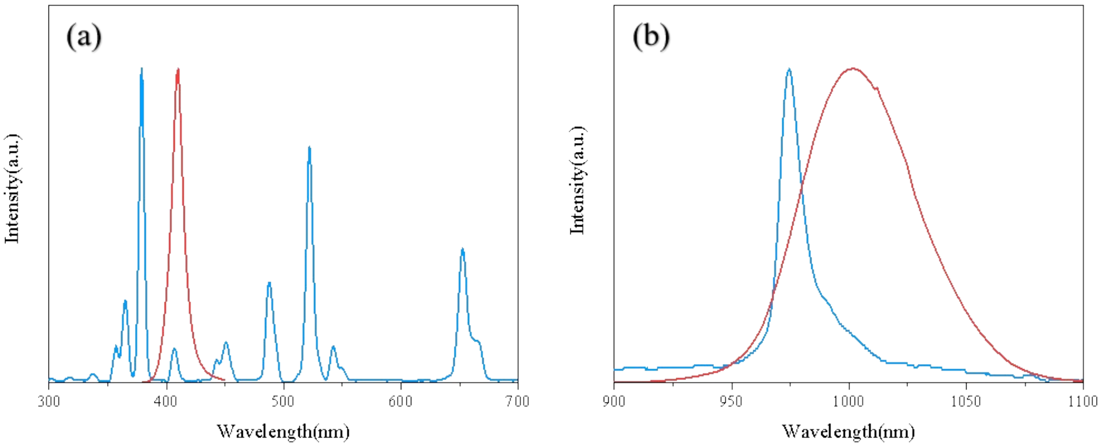

Fig. S10. (a) Absorption spectrum of Er^{3+} in $ErCl_3$ solution (blue) and emission spectrum of $CsPbCl_3$ NCs (red) in visible region; (b) Absorption spectrum of Er^{3+} in $ErCl_3$ solution (blue) and emission spectrum of Yb^{3+} in $CsPbCl_3$:Yb^{3+} NCs (red) in NIR region.

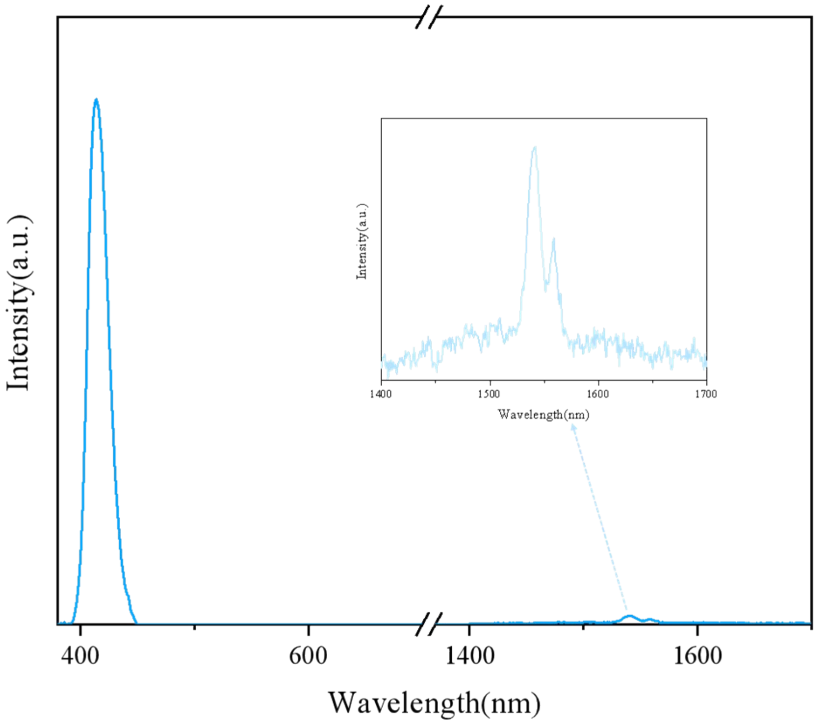

Fig. S11. PL spectrum of $CsPbCl_3:Er^{3+}$ NCs excited at 365 nm.

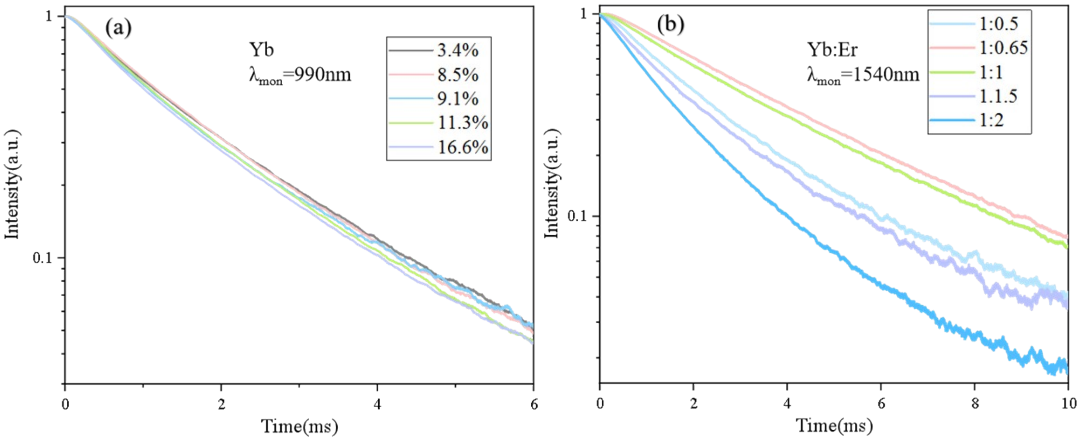

Fig. S12. The time-resolved PL of (a) $CsPbCl_3:Yb^{3+}$ (λ_{mon}=990nm) and (b) $CsPbCl_3:Yb^{3+}/Er^{3+}$ (λ_{mon}=1540nm) NCs excited at 365 nm. As the concentration of Er^{3+} increases, the lifetimes of $CsPbCl_3:Yb^{3+}/Er^{3+}$ (λ_{mon}=1540nm) NCs initially lengthen before experiencing a precipitous decline. This phenomenon is attributed to the quenching effect under high concentration of Er^{3+}.

Table S3. τ_{Yb}, $\tau_{Yb/Er}$ and ET efficiency (η_{ET}) from Yb^{3+} to Er^{3+} of different concentrations of Yb^{3+} or Er^{3+} in NCs.

$Yb^{3+}/Pb^{3+}+Yb^{3+}$	3.4%	8.5%	9.1%	11.3%	16.6%
τ_{Yb}(ms)	1.7	1.58	1.56	1.51	1.5

$Er^{3+}/Pb^{3+}+Er^{3+}+Yb^{3+}$	1.6%	3.6%	5.7%	6.3%	6.9%
$\tau_{Yb/Er}$(ms)	1.26	1.02	0.95	0.87	0.68
η_{ET}(%)	20.3	35.4	39.9	44.9	60

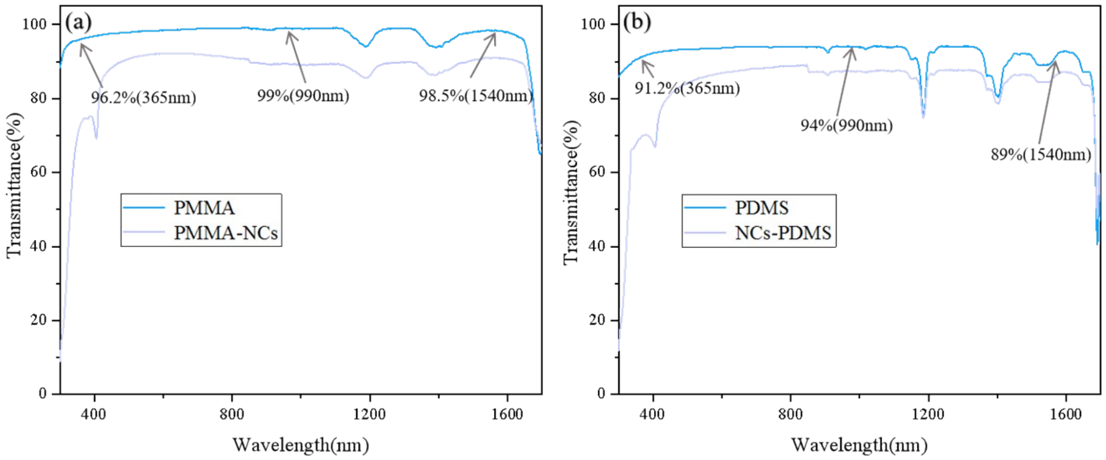

Fig. S13. Transmittance of (a) PMMA and (b) PDMS at the wavelengths of 365 nm, 990 nm, and 1540 nm before and after doping of NCs.

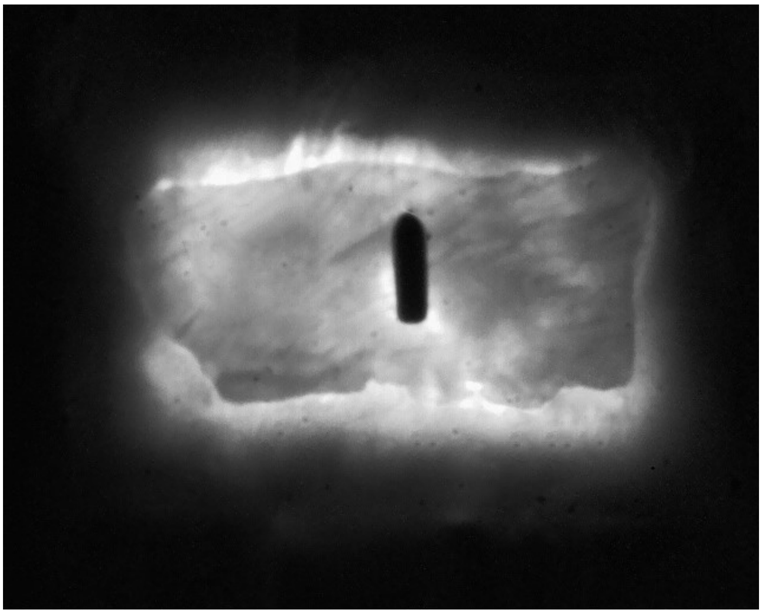

Fig. S14. Subcutaneous tissue (6.5mm) imaging by NIR camera.

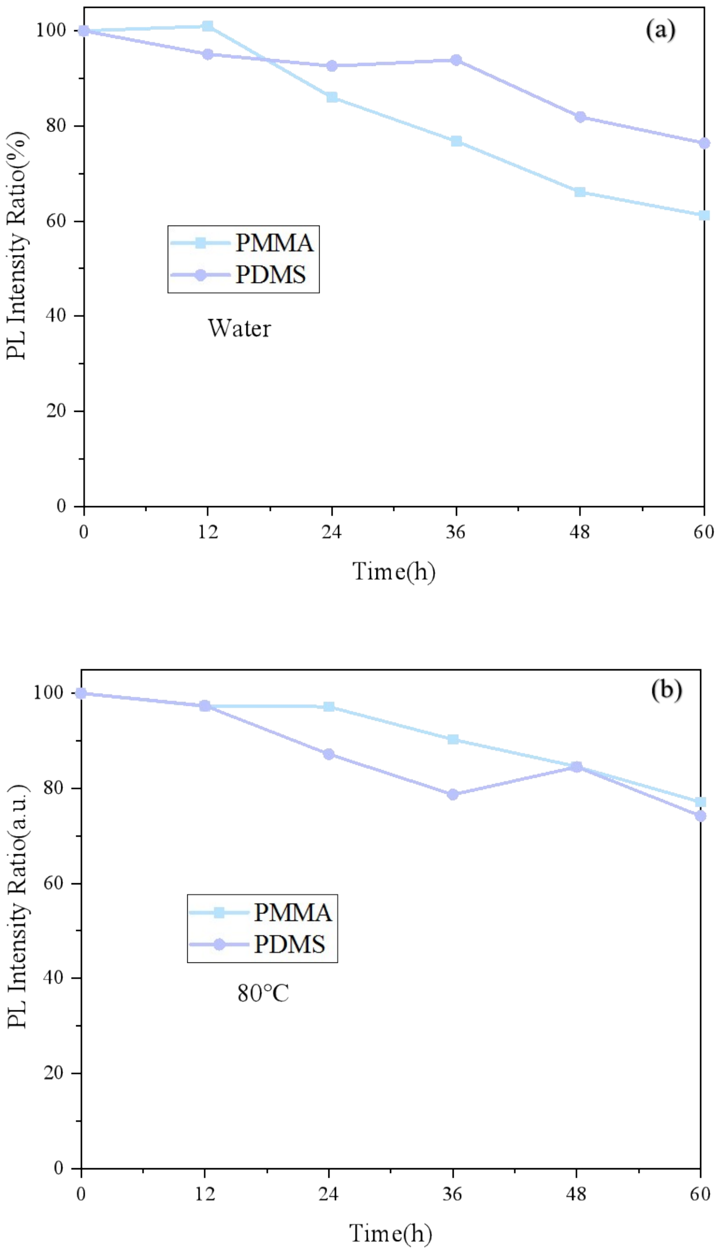

Fig. S15. (a) Water and (b) thermal stability under the encapsulation of PMMA or PDMS.

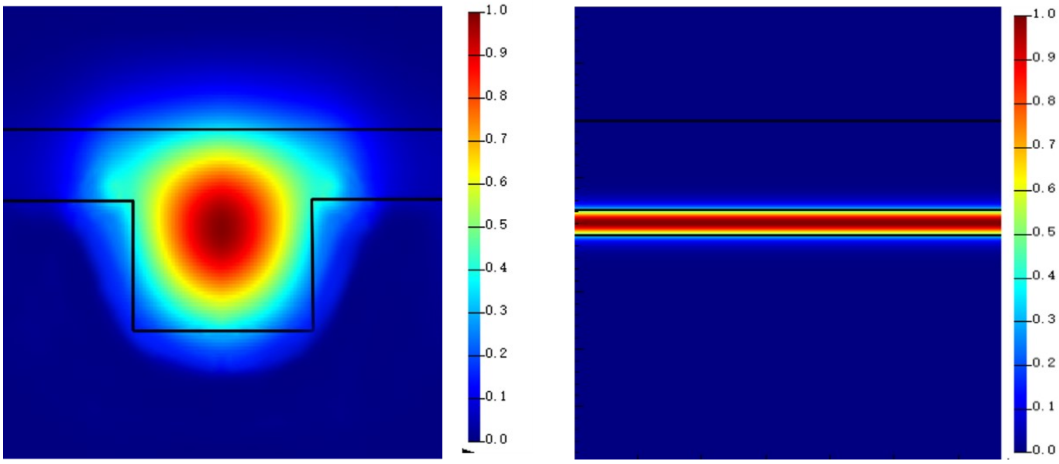

Fig. S16. Simulated optical field images of the input cross-section and longitudinal waveguide profile are presented. The 1540 nm signal light can be clearly observed to be almost entirely confined within the core region of the waveguide. The refractive indices are 1.455 for the cladding, 1.491 for the waveguide core, and 1.48 for the pure PMMA coating layer above the waveguide. The calculated numerical aperture (NA) is 0.326, indicating that the fiber possesses strong light-gathering capability. The coupling efficiency was measured to be 72.4%, corresponding to a loss of 1.4 dB.

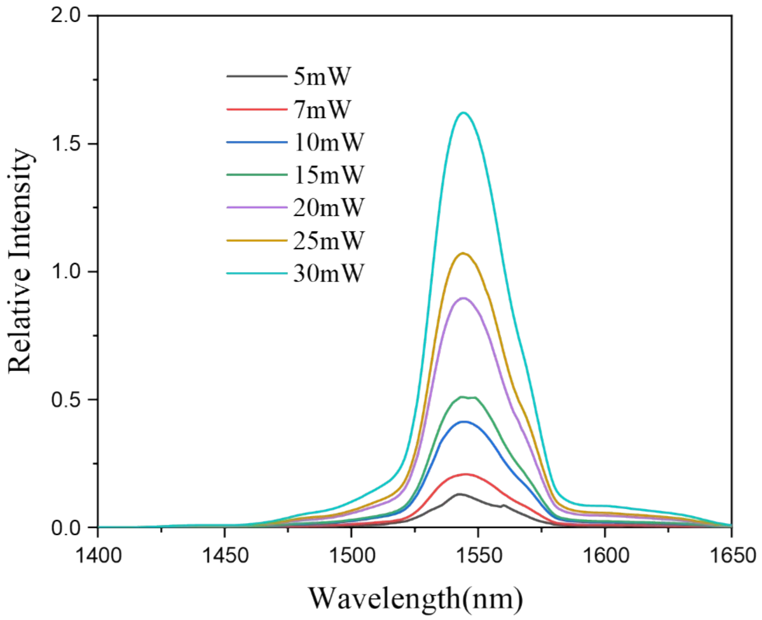

Fig. S17. Pump-power-dependent ASE background spectra.

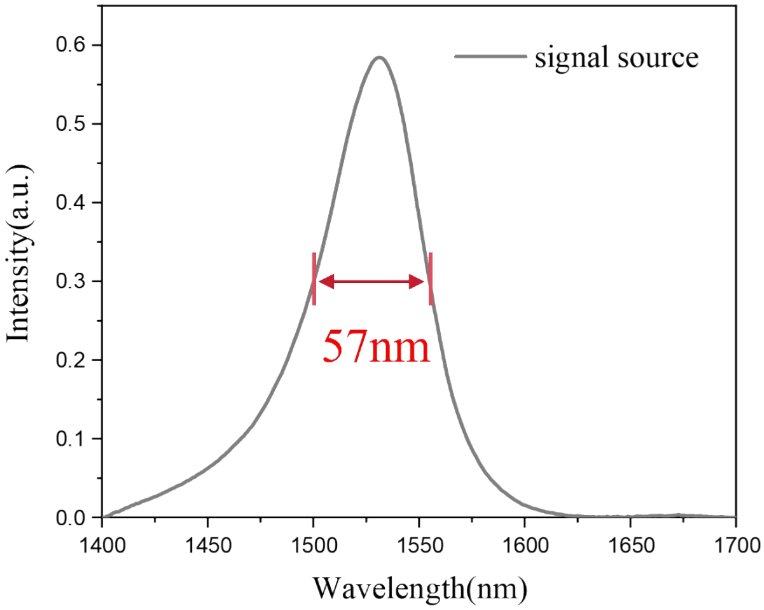

Fig. S18. Spectrum of the signal source and its linewidth.

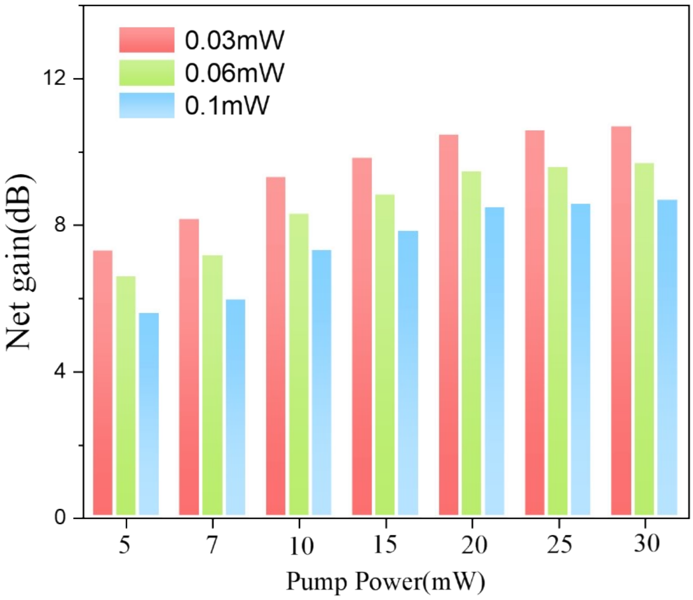

Fig. S19. Relative gains at 1540nm as functions of 365 nm pump power and 1540 nm signal power. The power of signal laser at the input waveguide facet is set at 0.03, 0.06, and 0.1 mW, respectively.

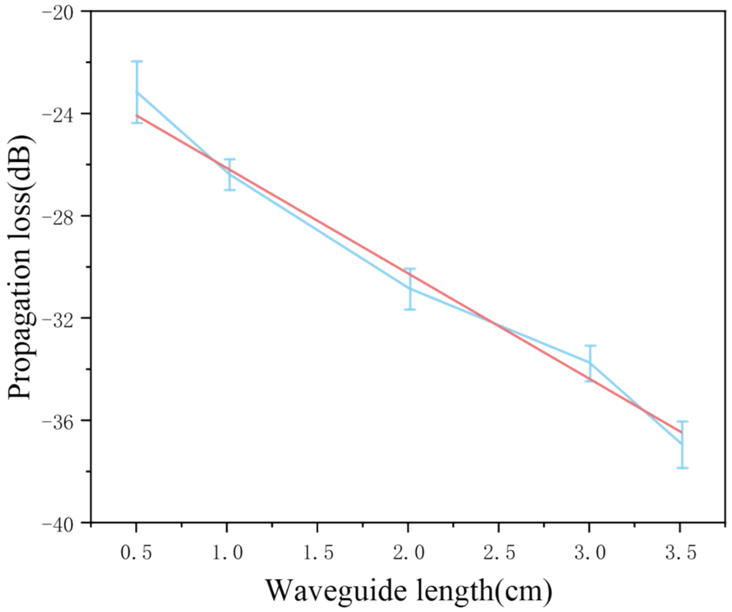

Fig. S20. The propagation losses at 1540nm of the waveguides with different lengths. The transparent loss is calculated using the formula: $\alpha = 10\log10(P_{in}/P_{out})/L$ where α is the loss coefficient (dB/cm), L is the length of the waveguide (cm), P_{in} is the input optical power, and P_{out} is the output optical power. It is calculated that α= 7.56 dB. After subtracting the measured propagation loss (4.76 dB/cm) and reflection loss (0.17 dB), the input and output coupling losses were accounted for at 1.4 dB each, owing to the identical coupling configuration.

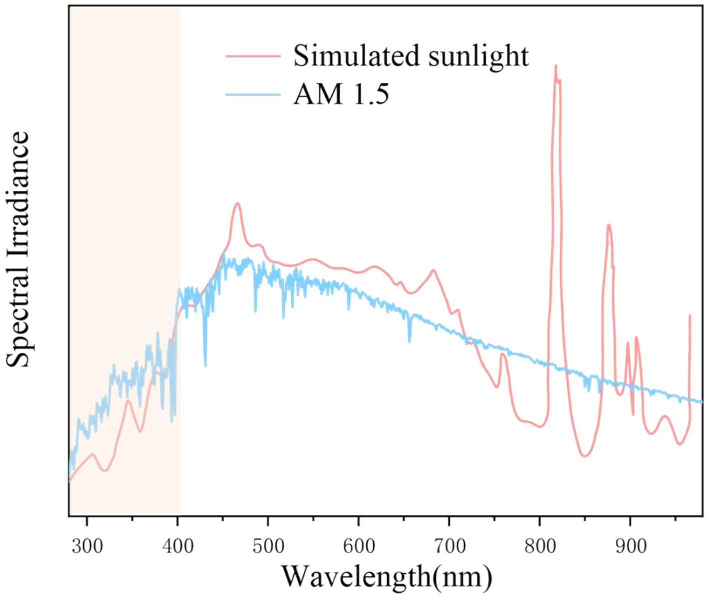

Fig. S21. Simulated sunlight and standard solar radiation AM1.5 spectra with the same irradiation power, wherein the portion absorbable by the waveguide is 280-405 nm, accounting for approximately 6% of the simulated sunlight or 8% of the actual sunlight.

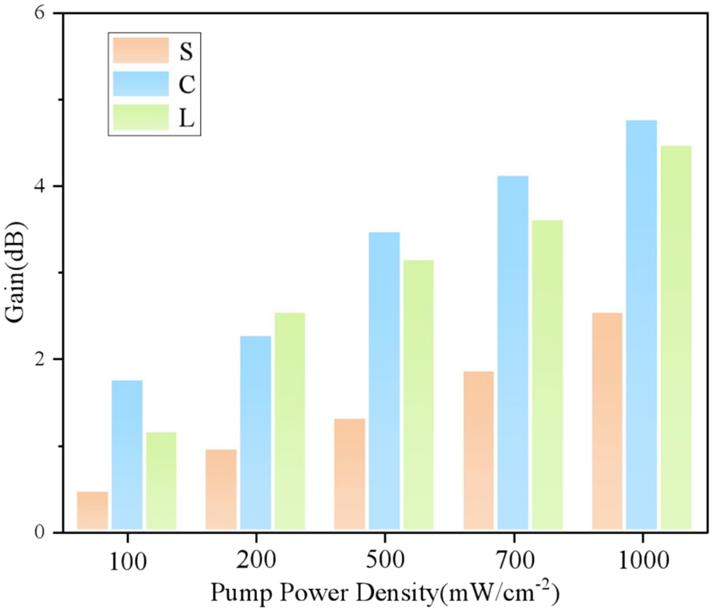

Fig. S22. The net gain at S, C and L band pumped by varying simulated sunlight pumping powers.

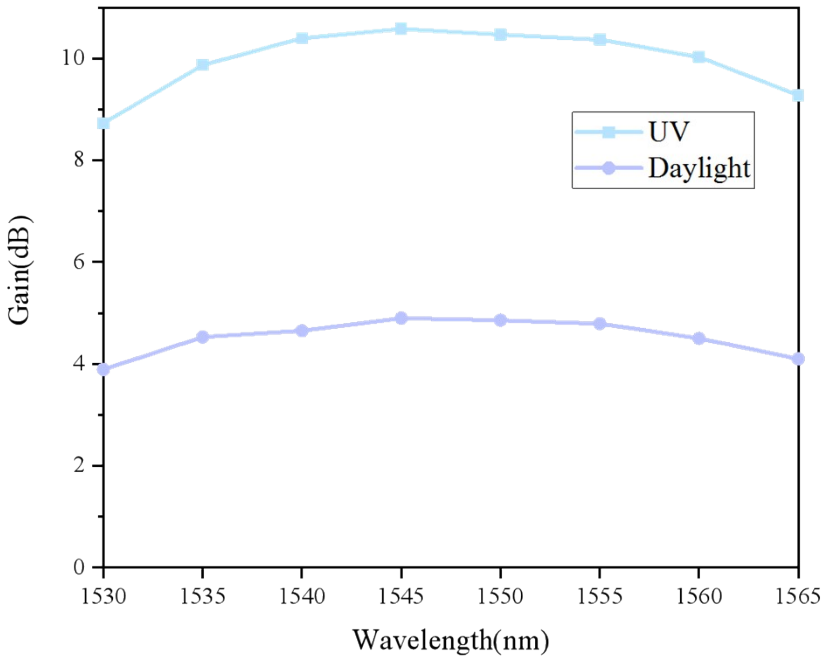

Fig. S23. Gain flatness under two different pumping sources in the C-band.

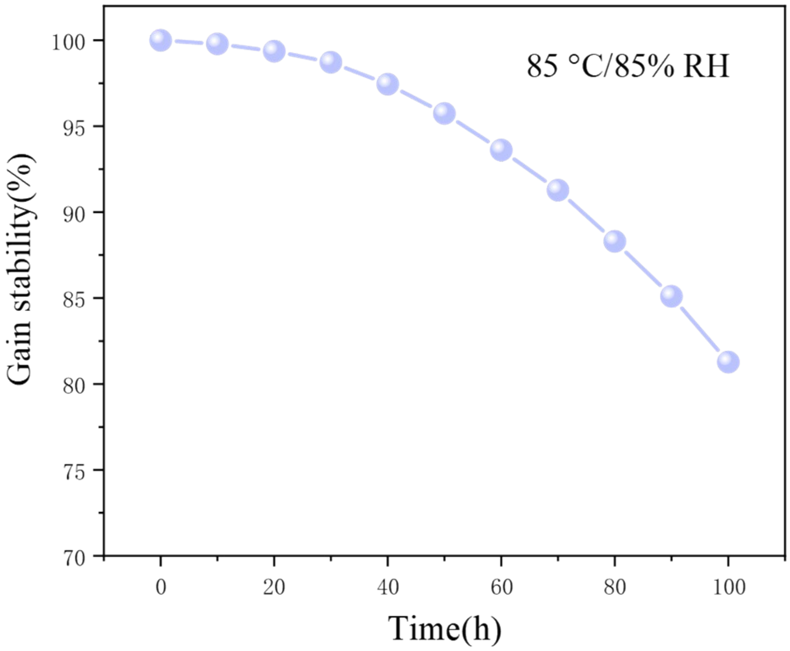

Fig. S24. Net gain stability in the 1540 nm band under simulated sunlight irradiation in an environment of 85 °C and 85% H.

References

[1] G. Kresse , Furthmüller J. Efficiency of ab-initio total energy calculations for metals and semiconductors using a plane-wave basis set, *Comp Mater Sci.*, 1996, **6** , 15.

[2] J. P. Perdew, Burke K, Ernzerhof M. Generalized gradient approximation made Simple, *Phys Rev Lett.*, 1996, **77** , 3865.

[3] P. E. Blochl, Projector augmented-wave method, *Phys Rev B Condens Matter*, 1994, **50** , 17953.

[4] S. Grimme , Semiempirical GGA-type density functional constructed with a long-range dispersion correction, *J Comput Chem.*, 2006, **27** , 1787.

[5] C. G. Van de Walle, J. Neugebauer, *J. Appl. Phys.*, 2004, **95**, 3851.

[6] Y. Zhu , G. Pan , L. Shao , G. Yang , X. Xu , J. Zhao and Y. Mao , *J. Alloys Compd.*, 2020, **835** , 155390.

[7] D. Li and G. Chen , *J. Phys. Chem. Lett.*, 2023, **14** , 2837.

[8] M. Zeng , F. Artizzu , J. Liu , S. Singh , F. Locardi , D. Mara , Z. Hens , R. V. Deun , *ACS Appl. Nano Mater.*, 2020, **3** , 4699.

[9] H. Li , X. Liu , D. Zhou , B. Dong , L. Xu , X. Bai and H. Song , *Adv. Mater.*, 2023, **35** , 2300118.